Supporting Information

to

Probing Fragment Ion Reactivity Towards Functional Groups on Coordination Polymer Surfaces

Markus Rohdenburg,*[a] Sebastian Kawa,[a] Maegan Ha-Shan,[a] Manuela Reichelt,[a] Harald Knorke,[a] Reinhard Denecke,[a] and Jonas Warneke*[a,b]

[a] *Wilhelm-Ostwald-Institut für Physikalische und Theoretische Chemie, Universität Leipzig, Linnéstr. 2, 04103 Leipzig, Germany.*
[b] *Leibniz Institute of Surface Engineering (IOM), Permoserstraße 15, 04318 Leipzig, Germany.*

Content

1. Regioselective binding of superelectrophilic anions to co-deposited reagents upon ISL

To explore whether superelectrophilic ions of type $[B_{12}X_{11}]^-$ selectively bind to C-H groups of deliberately co-deposited reagents (not only to those of ubiquitous background molecules), we soft-landed 4.7×10^{13} $[B_{12}I_{11}]^-$ ions onto a pre-deposited surface layer formed by soft-landing of 3.1×10^{13} *para*-vinylbenzenesulfonate ([*p*-VBS]$^-$, $[C_8H_7SO_3]^-$, see Figure S1) ions on a fluorinated self-assembled monolayer (FSAM) surface. Note that soft-landing of a sulfonate is expected to result in partial re-protonation on the surface so that the neutral acid *p*-VBSH may be formed. Note that due to the high electrophilicity of the $[B_{12}I_{11}]^-$ anion, it preferentially reacts with nucleophilic sites. Also, anion-anion reactions are possible at surfaces because the long-range Coulomb repulsion is compensated by the polarization of the grounded surface.[1]

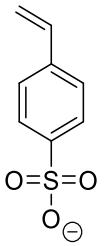

*Figure S1. Structure of [*p*-VBS]$^-$.*

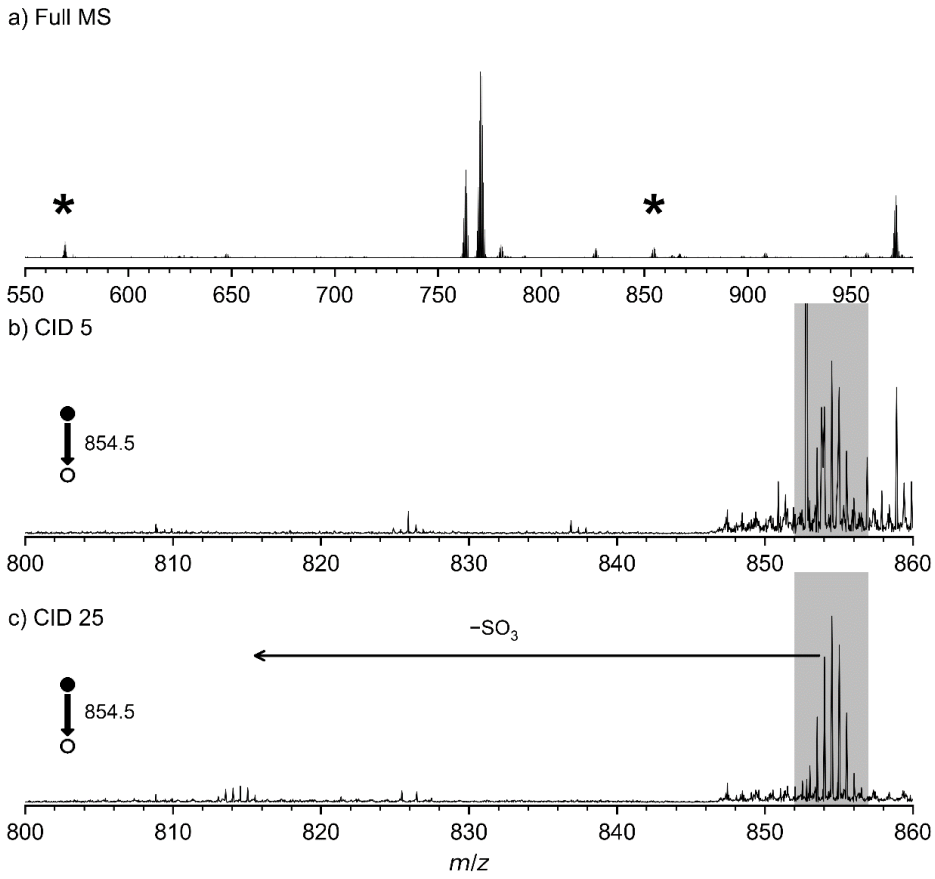

*Figure S2. a) −ESI mass spectrum acquired during LESA of the surface layer formed by sequential deposition of [*p*-VBS]$^-$ and $[B_{12}I_{11}]^-$. The signals, which are assigned to products formed by bond formation between both soft-landed species are marked with asterisks. Below: MS^2 spectra obtained after isolation and subsequent fragmentation of $[B_{12}I_{11}(C_8H_7SO_3)]^{2-}$ ions (m/z 854.5) upon CID with a collision energy of b) 5 V and c) 25 V. Note that in contrast to all other experiments reported herein, a Bruker Impact II (Bruker Daltonik, Bremen, Germany) mass spectrometer was used.*

The −ESI mass spectrum obtained during LESA of the resulting layer (Figure S2a) shows two signals that can be assigned to reaction products between $[B_{12}I_{11}]^-$ and *p*-VBS^-: $[B_{12}I_{11}(C_8H_7SO_3)]^{2-}$ (*m/z* 854.5) and $[B_{12}I_{11}(C_8H_6SO_3)]^{3-}$ (*m/z* 569.4). The presence of the latter signal suggests that the acidic -SO_2OH group of *p*-VBSH is still present in the adduct and can be deprotonated during the −ESI process. Note that the signals not marked with an asterisk in Figure S2a can be assigned to typical products that form by reaction of $[B_{12}I_{11}]^-$ with background molecules present during ion soft-landing at the layer interface (see ESI section 10). We further explored $[B_{12}I_{11}(C_8H_7SO_3)]^{2-}$ ions by CID experiments. While stable against fragmentation at low collision energies (Figure S2b), the ions eliminate sulfur trioxide (SO_3, 80 u) at higher collision energies (Figure S2c). Elimination of SO_3 is known from CID experiments with protonated organic sulfonic acids[2] thus confirming that binding of $[B_{12}I_{11}]^-$ occurred via substitution of a proton in a C-H bond and not by substitution of the proton in the sulfonic acid group. However, according to DFT calculations, binding to oxygen (Figure S3 left) is predicted to be thermochemically most favorable compared to proton substitution at the vinyl or aryl positions (Figure S3, middle and right). Therefore, the binding motif evidenced by mass spectrometric analysis may be explained by the *p*-VBSH surface orientation with its polar sulfonic acid group pointing towards the polarizable layer and the non-polar alkyl/aryl moiety being exposed to the vacuum. Note that direct addition of $[B_{12}I_{11}]^-$ to *p*-VBSH (without proton substitution) yielding a singly charged adduct was not observed experimentally. We thus decided to exclude respective species from the computational study. Note that Figure S3 shows calculated ion pairs consisting of a doubly charged molecular ion and a proton, which remains (electrostatically) bound to the dianions in our calculations. The ion pair can dissociate in the condensed phase yielding the detected dianions.

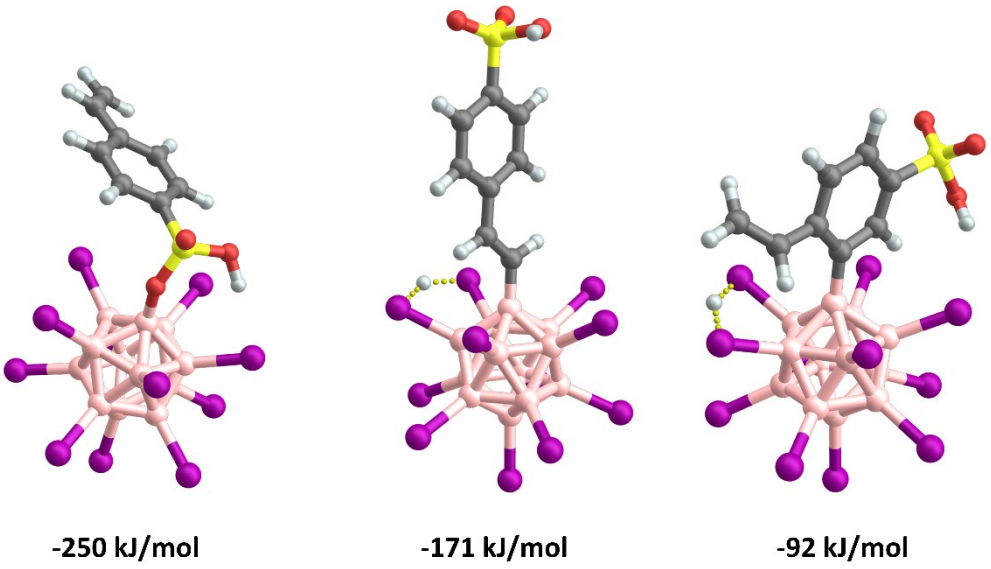

Figure S3. DFT optimized structures and BSSE-corrected 0K enthalpies for the binding of $[B_{12}I_{11}]^-$ to p-*VBSH. Three ion pairs resulting from substitution of a proton with $[B_{12}I_{11}]^-$ were considered with the substituted proton remaining electrostatically bound to the resulting doubly charged product. Note that no complete computational study of all possible isomers was performed. Rather, typical bonding motifs resulting from addition to the sulfonic acid group (left), substitution of a proton in the vinyl group (middle) or the aryl group (right) were assessed.*

2. Experimental and computational procedures

2.1. Chemicals

Copper(II) acetate monohydrate (purity: ≥98%), ruthenium(II) tris(bipyridine) chloride hexahydrate, 11-mercaptoundecanoic acid (MUDA) (purity: 95%), trimesic acid (H_3btc) (purity: 95%) and 5-methylisophthalic acid (H_2MeIp) (purity: 97%) were purchased from Sigma Aldrich. $K_2[B_{12}I_{12}]$ was obtained from the Jenne group (University of Wuppertal), where it was synthesized according to published literature procedures.[3,4] Ethanol for SurMOF preparation was purchased from Fisher Scientific (purity: 99.8%). All chemicals were used without further purification.

2.2. Preparation of surface-grown $Cu_3(btc)_2$ coordination polymer

Details about the layer-by-layer (LbL) preparation of $Cu_3(btc)_2$ have been described previously.[5,6] In brief, we employed silicon wafers (1×1 cm^2) covered with a 30 nm thick gold adlayer that is bound to the underlying Si surface via a 5 nm thick chromium adhesion layer (Siegert Wafer GmbH, Aachen, Germany) as substrates. These substrates were cleaned by successively immersing the sample in Millipore water and high purity ethanol under ultrasonication for at least five minutes. Subsequently, remaining contaminations were removed by combined UV/ozone cleaning (Ossila UV Ozone Cleaner L2002A, Ossila Limited, Sheffield, UK). The cleaned substrates were then immediately immersed into a 1 mM ethanolic solution of MUDA in which they were stored for 72 h for SAM formation. After thorough rinsing with EtOH, LbL preparation of $Cu_3(btc)_2$ was performed by alternately dipping the SAM-functionalized substrate in ethanolic solutions of copper(II) acetate monohydrate (0.1 mM) and H_3btc (0.1 mM) for 15 minutes each. Unless noted otherwise, a total number of 10 dipping cycles was performed. The substrate was thoroughly rinsed with EtOH in between each half cycle and additionally dried in a stream of N_2 after the last dipping cycle was terminated.

2.3. Ion Soft-Landing (ISL)

2.3.1. General procedures

The $Cu_3(btc)_2$-functionalized substrates were mounted into the sample holder of a recently introduced ion soft-landing instrument optimized for the deposition of fragment ions.[7] After the instrument was evacuated to reach a base pressure of 10^{-6}-10^{-5} mbar in the deposition region, an ESI source was used to transfer precursor ions into the gas phase. Herein, we employed solutions of (a) $K_2[B_{12}I_{12}]$ (0.1 mM in ACN) to generate **1**, and (b) $[Ru(bpy)_3]Cl_2$ (0.1 mM in MeOH) to generate **2** and supplied them to the ESI source. Two ion funnels operating at higher (high pressure funnel (HPF)) and lower (low pressure funnel (LPF)) pressures were employed to collimate and guide the ion beam from the source region to a rough vacuum stage. Following the dual ion funnel system, the ions enter a collision cell (CC) in which CID of the precursor ions was performed by applying a voltage difference to ion optics elements. After passing through the collision cell, ions enter a 90° bent ion guide (BIG), which facilitates separation of the ion beam from the stream of neutrals originating from the source. Subsequently, ions were mass-selected in the high vacuum region of the instrument by a quadrupole mass filter (QMF) based on their mass-to-charge ratio and afterwards are gently deposited (with kinetic energies in the range 5-10 eV/q) on the substrate placed directly behind the exit lens of the QMF. The substrate was held at room temperature and grounded via a picoammeter, with which the sample current was measured during deposition. The number of deposited ions was derived by integrating the current over time. For all experiments performed for this study, a total number of fragment ions in the range $6x10^{13}$-$5x10^{14}$ was

deposited, which – in previous studies – typically exceeded monolayer coverage when a sample surface area of 1x1 cm² is considered.[1,8] The deposition duration to achieve these coverages was typically in the range of 18-24 h. Note that for the purpose of functionalizing the $Cu_3(btc)_2$ surface, any coverage beyond a monolayer was assumed to be sufficient. All ion optics with the ion soft-landing instrument were powered and controlled by the MIPS control system developed by GAA Custom Electronics, LLC, and were adjusted to obtain a maximum ion current after mass selection. Applied RF voltages were adjusted to resonance frequencies of the electric LC circuits. All applied voltages and other setting for the deposition of **1** and **2** can be found in Table S1. All substrates were rinsed with 10 mL EtOH and dried in a stream of N_2 after they were removed from the ISL instrument.

2.3.2. Deposition parameters and settings

Table S1. Deposition parameters and settings.

Parameter	$[B_{12}I_{11}]^-$ (**1**)	$[Ru(bpy)_2]^{2+}$ (**2**)
Precursor	$K_2[B_{12}I_{12}]$	$[Ru(bpy)_3]Cl_2$
c (solution) / mM	0.10	0.10
flow rate / mL/h	0.10	0.10
U (ESI) / V	−3100	+2800
T (Inlet 1, 2) / °C	25	25
U (Inlet 1) / V	−400	+400
U (Inlet 2) / V	−400	+400
f (HPF) / kHz	676	676
U (HPF 1) / V	−430	+360
U (HPF 2) / V	−250	+310
U (HPF 3) / V	−240	+330
U (HPF 4) / V	−170	+150
p (HPF) / mbar	9.8	11.5
f (LPF) / kHz	881	881
U (LPF 1) / V	−151	+227
U (LPF lens) / V	−87	+80
U (LPF 2) / V	−105	+78
p (LPF) / mbar	3.2	6.5
f (CC) / kHz	1778	1778
U (CC bias) / V	−13.5	+0.3
U (CC lens) / V	−11.2	+5.3
p (CC) / mbar	$1\text{-}2\text{x}10^{-1}$	$1\text{-}2\text{x}10^{-1}$
f (BIG) / kHz	1773	1773
U (BIG bias) / V	−5.9	+5.3
U (BIG lens) / V	+7.0	+6.4
p (BIG) / mbar	$1\text{-}3\text{x}10^{-3}$	$1\text{-}3\text{x}10^{-3}$
f (QMF) / kHz	550	550
U (QMF in) / V	+120.0	−13.0
U (QMF pre) / V	+14.0	+0.5
U (QMF post) / V	+13.0	+2.0
U (QMF out) / V	−6.0	−1.0
U (QMF bias) / V	+12.0	−4.0
m/z	1504.0	206.0
R = (m/z)/Δ(m/z)	30 ± 3	5.4 ± 3
p (SL chamber) / mbar	$3.0\text{-}6.0\text{x}10^{-6}$	$7.0\text{-}10.0\text{x}10^{-6}$
KE/charge / eV/*q*	9.4	5.7

2.3.3. Kinetic energy measurements

Kinetic energy (KE) measurements were performed by the retarding potential method.[7] In brief, a metal double mesh was mounted in front of the deposition target. The mesh more remote to the target was kept at ground potential and the mesh closer to the target was set to a variable retarding potential. This setup allows for a homogeneous electric field in between both meshes. To perform the KE measurements, the ion current was measured from the deposition target while the retarding potential was varied in steps of 0.1 V. The ion current was then plotted as a function of the retarding potential. We performed five single scans under identical conditions and averaged the resulting data points. The averaged plot was then fitted with a sigmoidal distribution with asymmetry with respect of the slope on both sides of the inflection point. We then analytically calculated the first derivative of the sigmoidal curve and normalized its integral yielding a probability density function for the KEs per charge with which the ions were deposited. The maximum of the probability density function was annotated next to the curve. Figures S4 and S5 show the results for **1** (maximum of the density function at 9.4 eV/*z*) and **2** (maximum of the density function at 5.7 eV/*z*), respectively. In all cases, settings were kept at the values reported in Table S1.

A central aim of the present study is the intact deposition of **1** and **2** on the $Cu_3(btc)_2$ surface. Former studies have shown that the formation of fragment ion reaction products that contain intact **1** and **2** is facilitated by deposition of **1** with a kinetic energy of up to 20 eV/z[1] and by deposition of **2** with a kinetic energy of up to 25 eV/z,[9] respectively. The kinetic energies measured for deposition of **1** and **2** in the present study should thus ensure that large quantities of deposited ions stay intact upon contact with the $Cu_3(btc)_2$ interface and are available for bond formation.

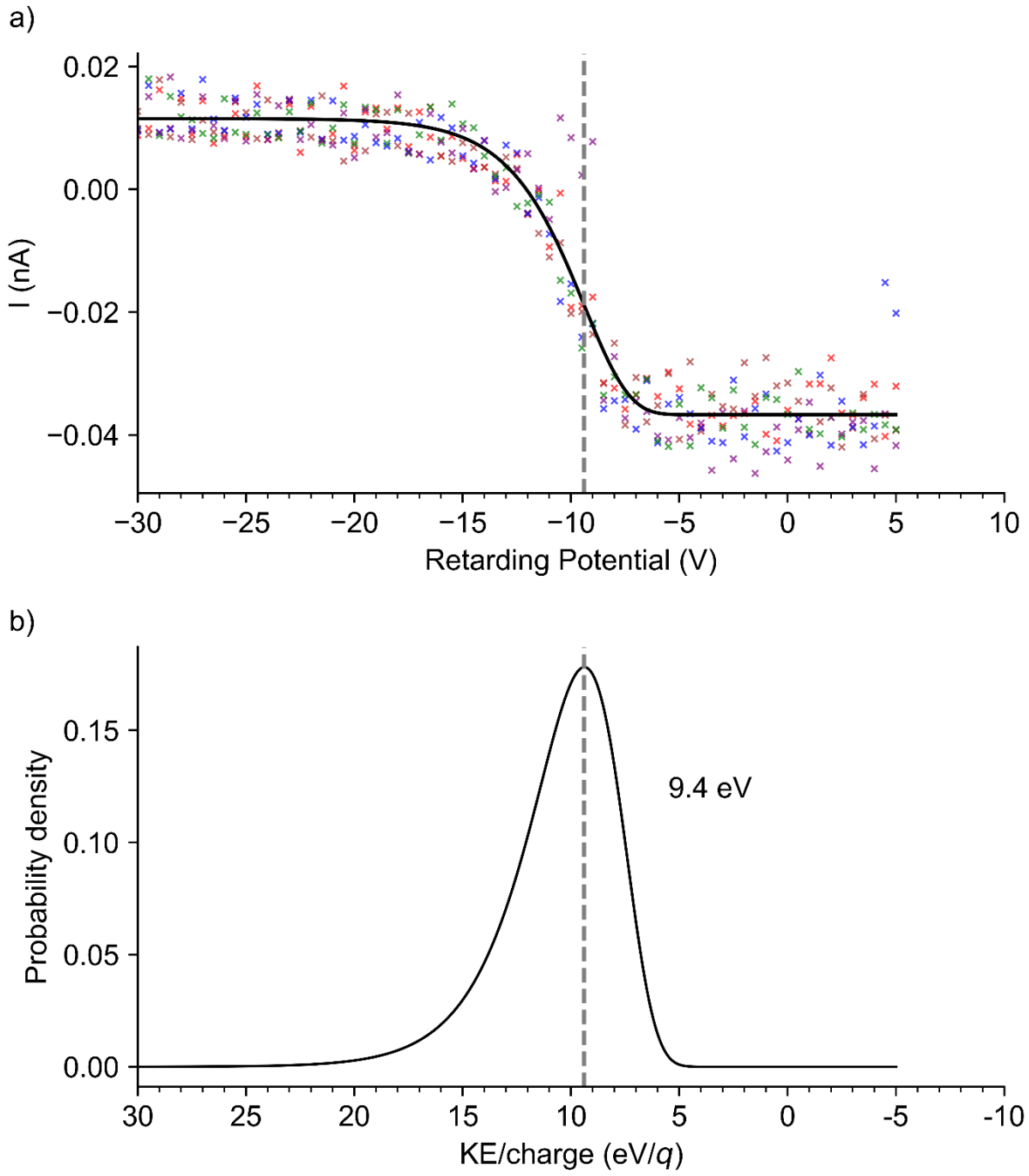

Figure S4. a) Ion current of $[B_{12}I_{11}]^-$ as measured on the deposition target as a function of the retarding potential. Five separate experiments under identical conditions were performed (individual data points are shown as "X" in a color representative for a single experiment) and all data was subsequently averaged and fitted by a sigmoidal function (black line). The position of the inflection point is marked with a dashed grey line. b) Probability density function for the KE per charge (q) obtained by calculating the first derivative of the sigmoidal function in a). The position of the maximum is marked with a dashed grey line.

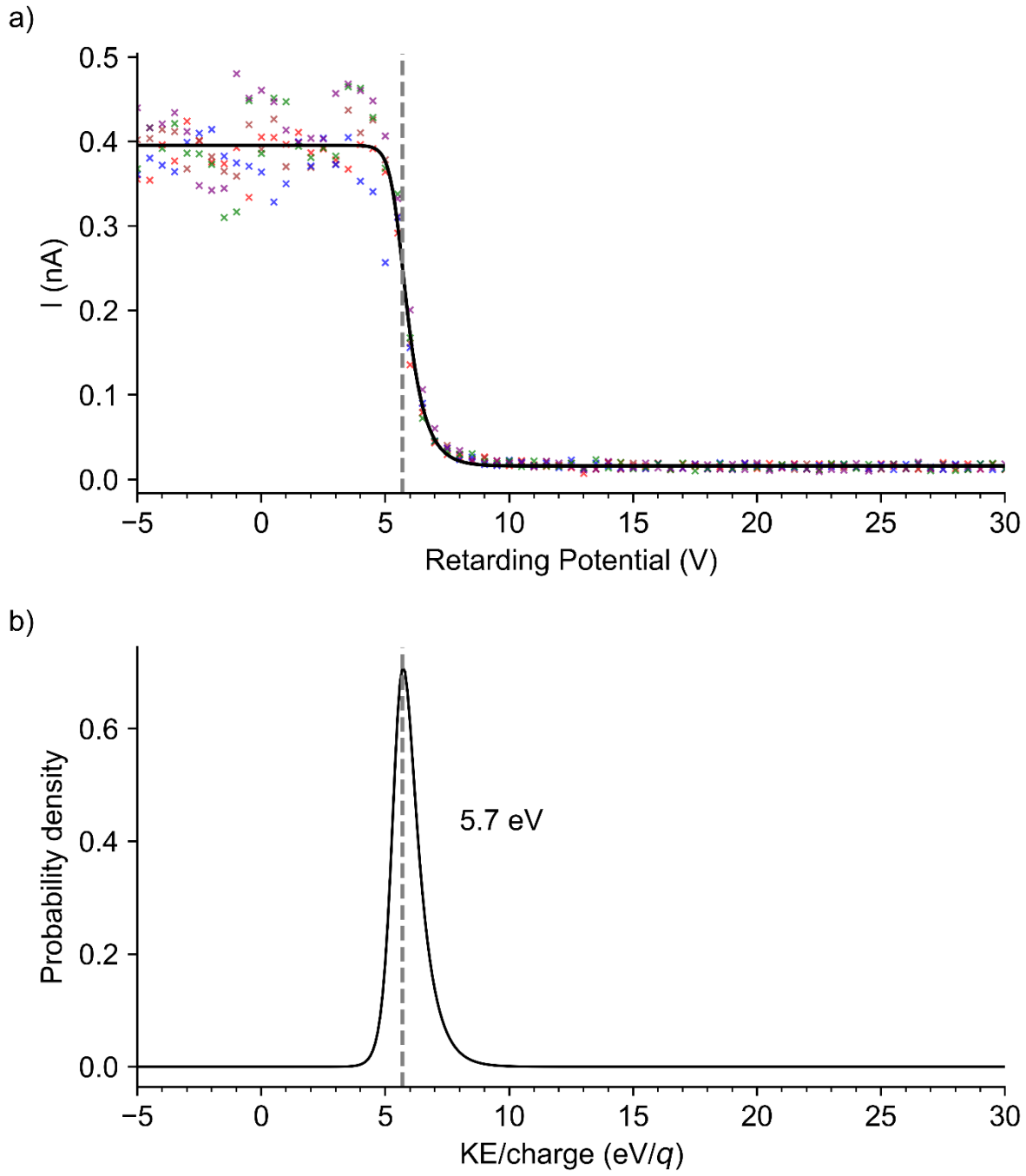

Figure S5. a) Ion current of $[Ru(bpy)_2]^{2+}$ as measured on the deposition target as a function of the retarding potential. Five separate experiments under identical conditions were performed (individual data points are shown as "X" in a color representative for a single experiment) and all data was subsequently averaged and fitted by a sigmoidal function (black line). The position of the inflection point is marked with a dashed grey line. b) Probability density function for the KE per charge obtained by calculating the first derivative of the sigmoidal function in a). The position of the maximum is marked with a dashed grey line.

2.4. Reflection-Absorption Infrared Spectroscopy (RAIRS)

RAIR spectra were acquired with an evacuated FTIR spectrometer (Vertex 70v, Bruker Optics GmbH) equipped with a grazing incidence reflection unit and a liquid nitrogen-cooled MCT detector (sensitivity limit down to 750 cm^{-1}). Spectra were collected from 4000 to 750 cm^{-1} with a resolution of 4 cm^{-1} and an aperture of 3 mm by averaging 1000 single scans. The sample chamber was evacuated to <1 mbar during measurements, while the system was purged with N_2 during sample mounting. All spectra were measured against a MUDA-SAM-functionalized Au substrate as a background sample, unless noted otherwise.

2.5. Liquid Extraction Surface Analysis (LESA) mass spectrometry

A TriVersa Nanomate (Advion) for Liquid Extraction Surface Analysis (LESA)[10] was used for nano-ESI analysis. A small portion of the layer (1 to 2 mm^2) was dissolved in 2 µL of (80:20 MeOH:H_2O *v*/*v*) and subjected to a subsequent chip-based nano-ESI analysis. This procedure minimizes the required sample volume and is highly sensitive. Unless noted otherwise, mass spectra were acquired on a Thermo Fisher LTQ XL Orbitrap spectrometer (Thermo Scientific GmbH, Bremen, Germany). The Nanomate device was also used to inject the ethanolic rinsing solutions into the instrument, this time by aspiring the liquid from a well plate in which the solutions were filled prior to analysis.

2.6. X-Ray Photoelectron Spectroscopy (XPS) and Ar^+ ion sputtering

XPS and the sputtering processes were carried out with an equipment dimensioned for UHV conditions (SPECS Surface Nano Analysis GmbH). The apparatus consists of a nonmonochromatic X-ray source (XR50) with an Al/Mg twin anode (Al K_α radiation was used here at 240 W source output) and a hemispherical energy analyzer (PHOIBOS 150-MCD9). All survey spectra were recorded as a single scan with an energy step width of 0.5 eV and a dwell time of 0.1 s, respectively. In contrast, the core level spectra were recorded as multiple scans with an energy step width of 0.1 eV and the same dwell time (0.1 s). The analyzer was operated in the fixed analyzer transmission mode (FAT) at a pass energy of 30 eV. Sputtering was performed only on the $[B_{12}I_{11}]^-$ on $Cu_3(btc)_2$ sample. Ar^+ ions were generated by means of an ion source (IQE 12/38) at 1000 V, 6 mA and an Ar pressure of $2x10^{-7}$ mbar. The sputtering duration was varied and is given as total sputtering time in the corresponding figures.

The XPS data were recorded with the software SPECSLAB 2 (version 2.44, SPECS Surface Nano Analysis GmbH). The data files were converted into the VAMAS format. For data evaluation the software UNIFIT 2024 (Unifit Scientific Software GmbH) was used. All contributions from X-ray satellites because of the use of the nonmonochromatic X-ray source were subtracted from the spectra (survey and core level spectra). In general, the core level spectra were fitted with a background function (sum of Shirley and second order polynom) and a peak function (Gaussian–Lorentzian convolution function). Unless otherwise stated the fitted background was subtracted from the shown core level spectra. To derive quantitative information, the signal intensities from the fitting process were normalized to the excitation cross section and corrected for experimental factors by applying sensitivity factors. The survey spectra were not fitted. The binding energy scale is given as measured and was not referenced to a standard value, respectively.

2.7. DFT calculations

DFT calculations were performed with the Gaussian 16, rev. C02 quantum chemistry software package.[11] Thermochemistry was assessed by subtracting the ZPE-corrected electronic energies of the reagents from those of the reaction products calculated on B3LYP/Def2-TZVPP[12–15] level including empirical dispersion corrections on D3 level with Becke-Johnson damping.[16,17] All reported structures were optimized and subsequently subjected to a frequency analysis that revealed the absence of any imaginary frequency. The Basis Set Superposition Error (BSSE) was accounted for by performing counterpoise calculations.[18,19] Resulting outputs from these calculations are published in ioChem-BD and can be accessed under the following link:

https://doi.org/10.19061/iochem-bd-6-337

3. Characterization of $Cu_3(btc)_2$ coordination polymer with RAIRS

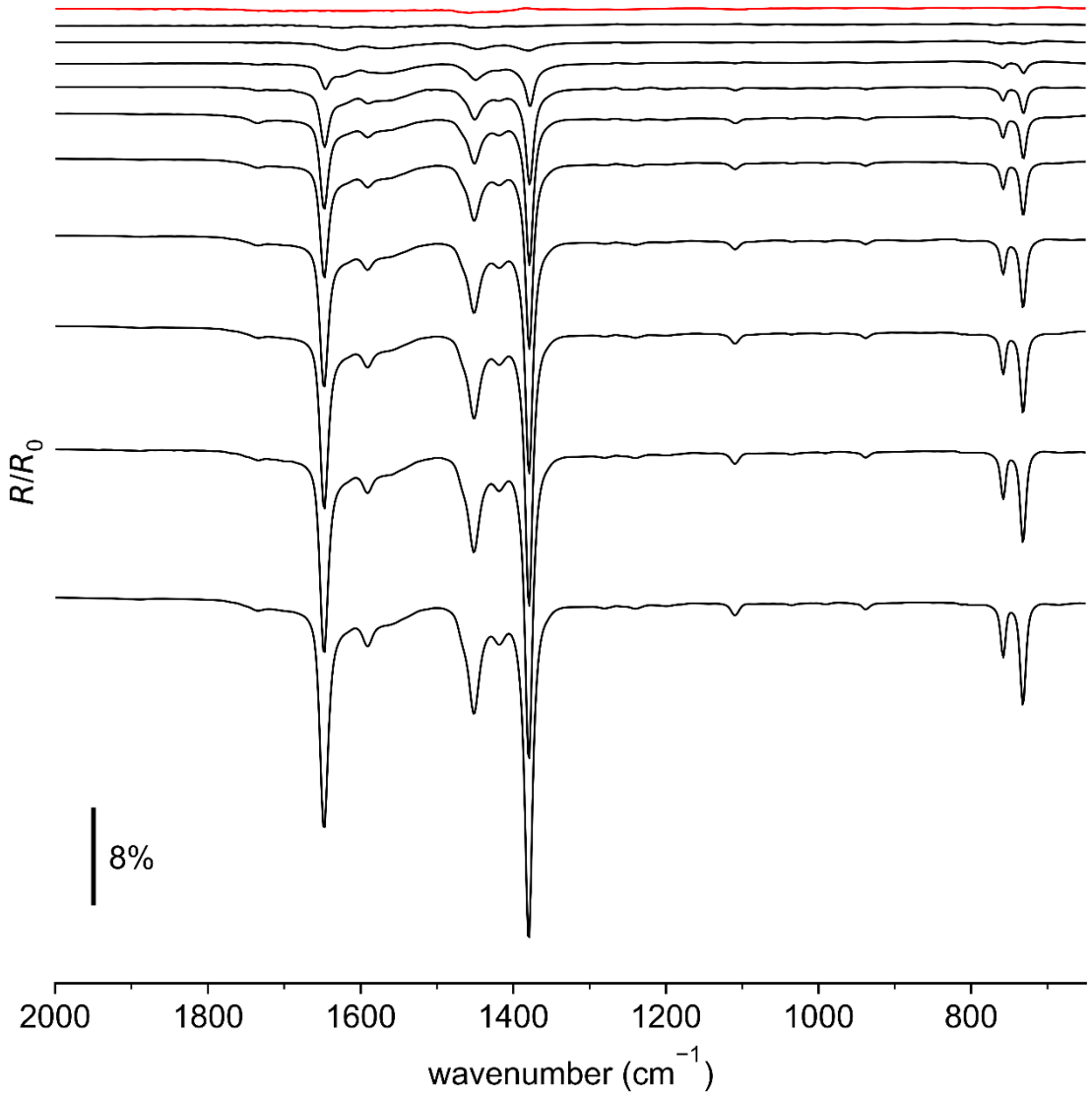

Figure S6. RAIR spectra acquired after every full LbL cycle during the growth of 10 layers of $Cu_3(btc)_2$ coordination polymer. The cycle number increases from top to bottom. The red spectrum in the top was acquired from the MUDA SAM (measured against a freshly cleaned Au surface as background sample) prior to the first LbL cycle.

Table S2. Assignment of the vibrational features of $Cu_3(btc)_2$ coordination polymer and comparison to the literature.

Exp. (cm^{-1})	Literature (cm^{-1})[20]	Assignment[20–23]
1735	1710	ν(COOH)
1648	1651	ν_{as}(COO)
1590	1580	ν(COO) – remaining $Cu_2(ac)_4$
1451	1452	ν_{as}(COO)
1419	1419	ν_{s}(COO)
1380	1377	ν_{s}(COO)
1109	1109	δ(C-H) in-plane
938	938	δ(O-H)
758	759	ω(C-H)$_{arom}$
733	730	ω(C-H)$_{arom}$

4. LESA method for obtaining mass spectra from $Cu_3(btc)_2$ coordination polymers

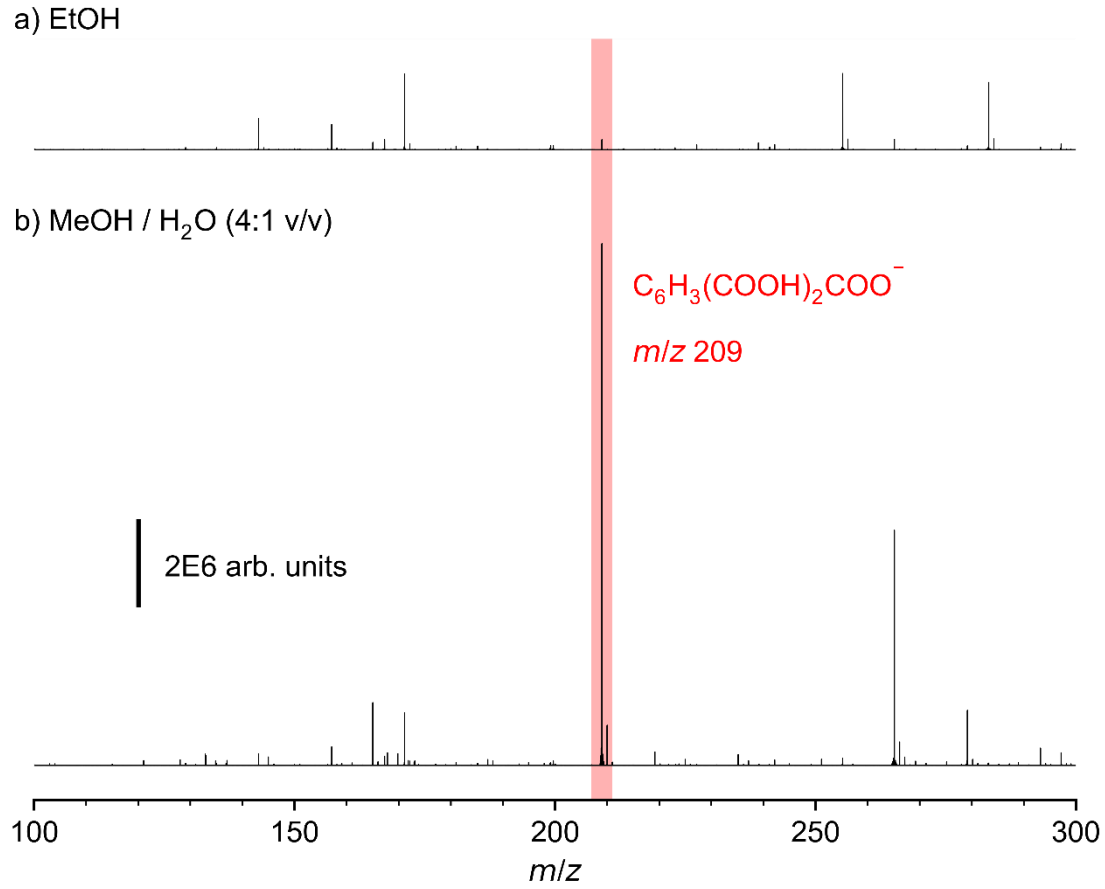

Figure S7. Mass spectra acquired with LESA from the same $Cu_3(btc)_2$ coordination polymer surface first (a) with 100% EtOH used as solvent and subsequently (b) with a solvent mixture containing MeOH and H_2O (4:1 v/v). The signal at m/z 209 (marked in red) can be assigned to the trimesate monoanion ($C_6H_3(COOH)_2COO^-$) and thus represents a measure for the amount of coordination polymer dissolved during LESA-MS. The vertical line in the lower left part serves as a measure for the intensity and is applicable for a) and b).

5. Quadrupole mass spectra demonstrating fragmentation

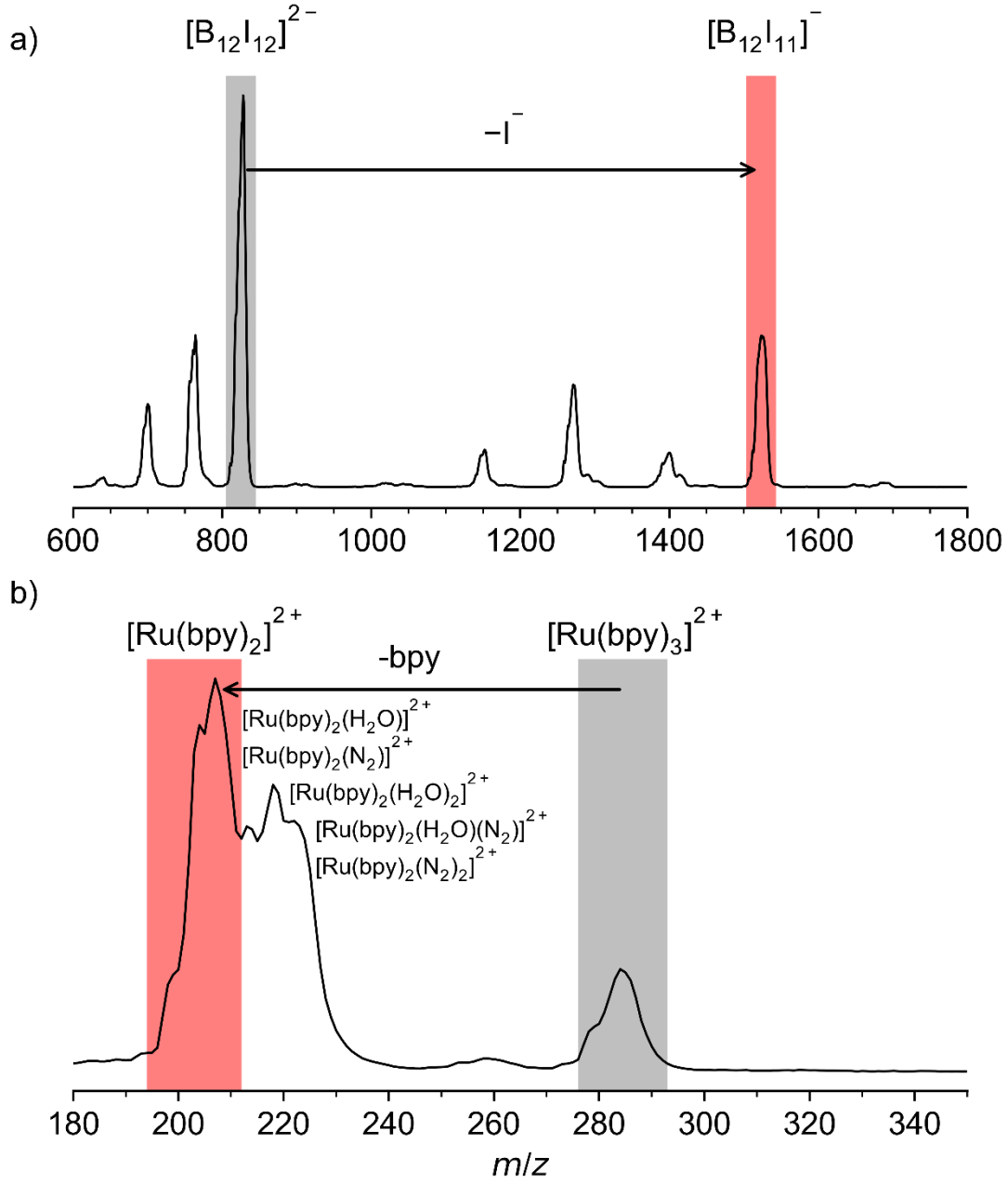

Figure S8. Mass spectra acquired with the quadrupole mass filter of the ion soft-landing instrument. Note that these mass spectra were acquired at the highest resolution available with the ISL instrument, i.e., *R = 100 ± 3 for **1**, and R = 20 ± 3 for **2**. a) Deposition parameters optimized for the deposition of $[B_{12}I_{11}]^-$, b) deposition parameters optimized for the deposition of $[Ru(bpy)_2]^{2+}$. Signals of respective precursor ions a) $[B_{12}I_{12}]^{2-}$, and b) $[Ru(bpy)_3]^{2+}$] are marked with a grey area, resulting fragment ion signals are marked with a red area. The eliminated ion/molecule is annotated next to the arrows. Note that the shoulder on the high-mass flank of the $[Ru(bpy)_2]^{2+}$ signal is likely caused by the formation of gas phase adducts of the highly reactive fragment ion with background gas molecules like N_2 and H_2O that replace the eliminated bpy ligand. At the mass resolution available in the ISL instrument, co-deposition of these adducts cannot be ruled out but due to the relatively weak bonds, likely **2** will be widely recovered upon collision with the surface.*

6. Mass spectra of rinsing solutions

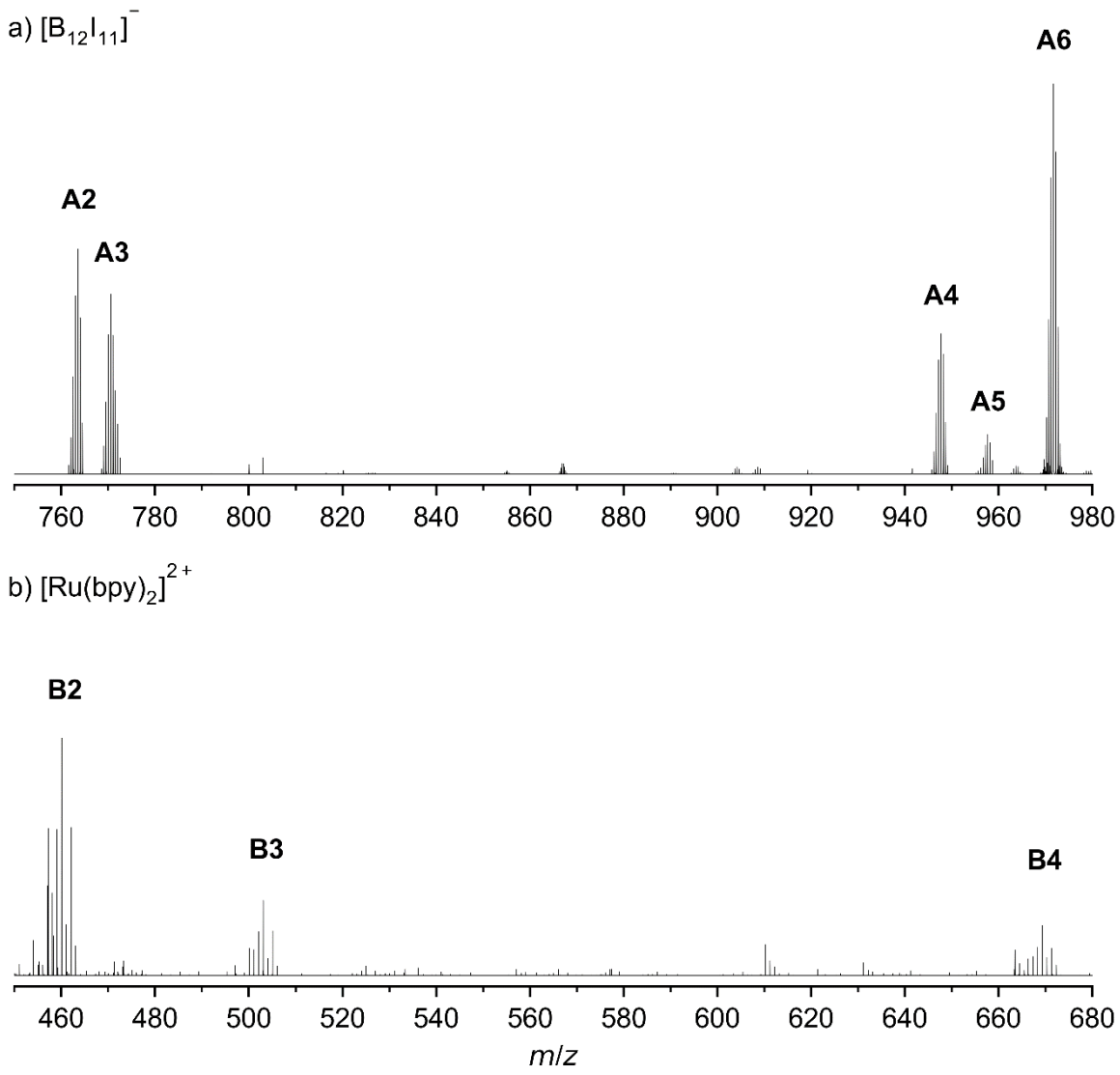

*Figure S9. Mass spectra acquired from a well plate with the LESA-MS setup from the ethanolic rinsing solutions obtained after ISL of a) **1** and b) **2**. For these mass spectra, the first 100 µL of EtOH were collected after dissolution of the products from the deposition surfaces and then introduced into the ESI source without further dilution.*

Table S3. Signal assignment of mass spectra of the EtOH rinsing solutions. m/z *values refer to most abundant signals from the isotopologue distribution.*

Signal	*m/z* (exp.)	*m/z* (sim.) [diff.]	Assignment
$[B_{12}I_{11}]^-$ (**1**)			
A2	763.5206	763.5385 (+0.0179)	$[B_{12}I_{11}H]^{2-}$
A3	770.5276	770.5463 (+0.0187)	$[B_{12}I_{11}(CH_3)]^{2-}$
A4	947.6635	947.6857 (+0.0222)	$[B_{12}I_{11}(C_4H_7(COOC_8H_{17})_2)]^{2-}$ (dioctyladipate adduct)
A5	957.6477	957.6692 (+0.0215)	$[B_{12}I_{11}(C_6H_3(COOC_8H_{17})_2)]^{2-}$ (dioctylphtalate adduct)
A6	971.6625	971.6858 (+0.0233)	$[B_{12}I_{11}(C_6H_3(COOC_9H_{19})_2)]^{2-}$ (dinonylphtalate adduct)
$[Ru(bpy)_2]^{2+}$ (**2**)			
B2	460.0417	460.0342 (-0.0075)	$[Ru(C_{10}H_8N_2)_2NO_2]^+$ (nitrite adduct)
B3	503.0733	503.0659 (-0.0074)	$[Ru(C_{10}H_8N_2)_2C_3H_5O_3]^+$ (lactate adduct)
B4	669.2854	669.2748 (-0.0106)	$[Ru(C_{10}H_8N_2)_2C_{16}H_{31}O_2]^+$ (palmitate adduct)

7. RAIR spectra after ISL of fragment ions on $Cu_3(btc)_2$ surfaces

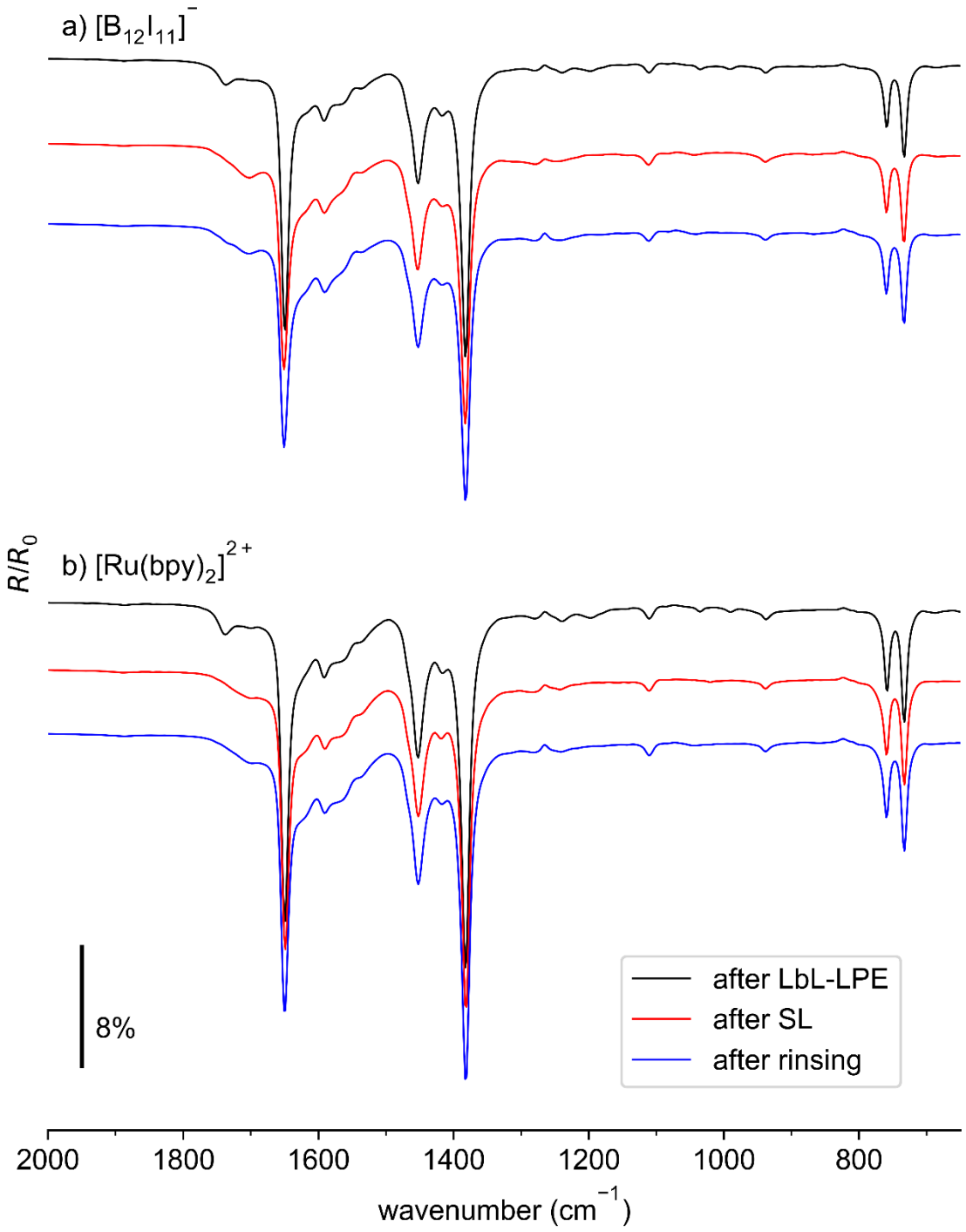

Figure S10. RAIR spectra acquired after different process steps (black: after LbL preparation of 10 layers of $Cu_3(btc)_2$ coordination polymer, red: after soft-landing of a certain fragment ion, blue: after rinsing of the $Cu_3(btc)_2$ sample with 10 mL EtOH) of the functionalization of $Cu_3(btc)_2$ coordination polymer surfaces with a) $[B_{12}I_{11}]^-$ and b) $[Ru(bpy)_2]^{2+}$ fragment ions.

Additional vibrational features after ISL due to the presence of the deposited fragment ions or their reaction products were not observed in RAIRS. However, in all cases, a shift of the band at 1735 cm^{-1} that can be assigned to C=O stretches in residual COOH groups of the pristine coordination polymer (*i.e.*, likely the terminating groups at the vacuum interface after LbL preparation) to 1703 cm^{-1} was observed. Aging effects of the samples kept under ambient conditions can be held responsible for this shift since it was also observed for a sample that was not subjected to ISL but stored under the same conditions for six days (see next ESI section). RAIRS also showed no changes beyond the described aging effect after the EtOH rinsing step. The absence of vibrational features due to the presence of the deposited ions can be rationalized by considering that the underlying $Cu_3(btc)_2$ substrate with a thickness of 10 layers and the presence of many carboxylate groups with intense IR absorption give rise to RAIRS intensities exceeding 20% (R/R_0) on its major vibrational features. For ISL deposit layers composed of ions similar to **1**, we obtained in former studies[8] RAIRS intensities of the major vibrational features in the sub-1% (R/R_0) range when coverages of $4x10^{14}$ ions were analyzed (nearly corresponding to the highest coverages used in the present study prior to rinsing). We therefore conclude that the RAIR spectra are too dominated by the btc vibrational features, and the amount of deposited fragment ions is too little to account for visible spectral changes.

8. RAIR spectra after storage of $Cu_3(btc)_2$ coordination polymer substrates

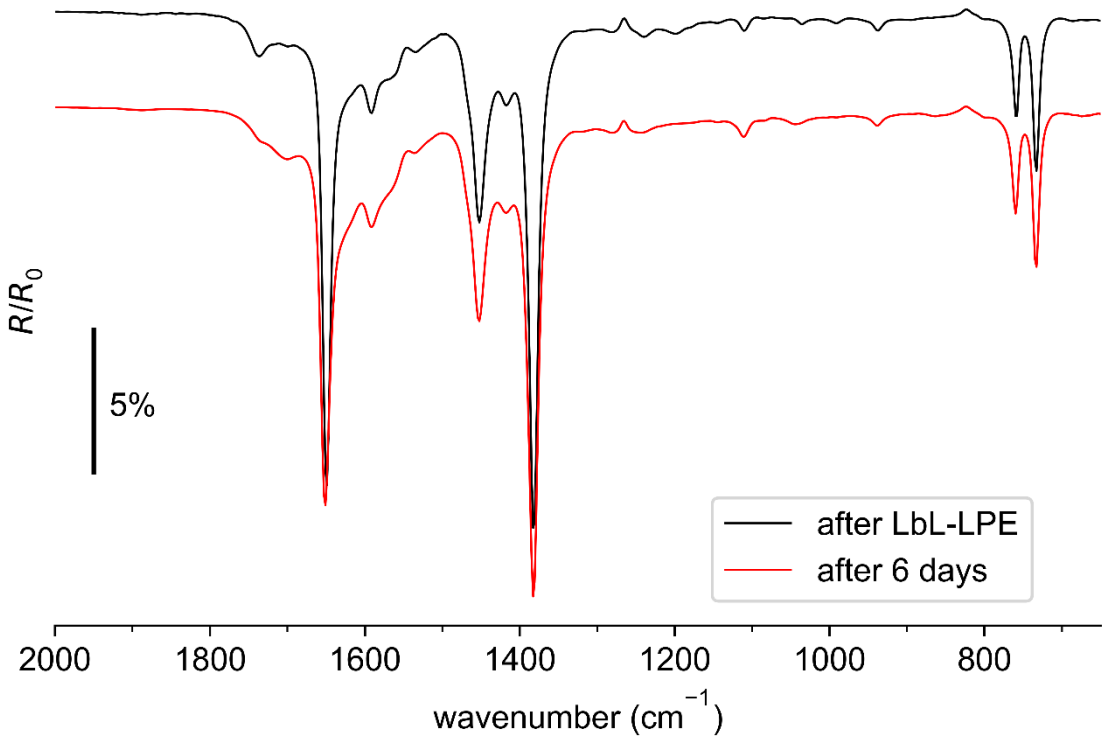

Figure S11. RAIR spectra acquired after different aging stages of a 10-layer $Cu_3(btc)_2$ coordination polymer. Black: after LbL preparation of 10 layers of $Cu_3(btc)_2$ coordination polymer, red: same sample after a storage period of six days under ambient conditions.

9. Additional XPS and Ar^+ ion sputtering data

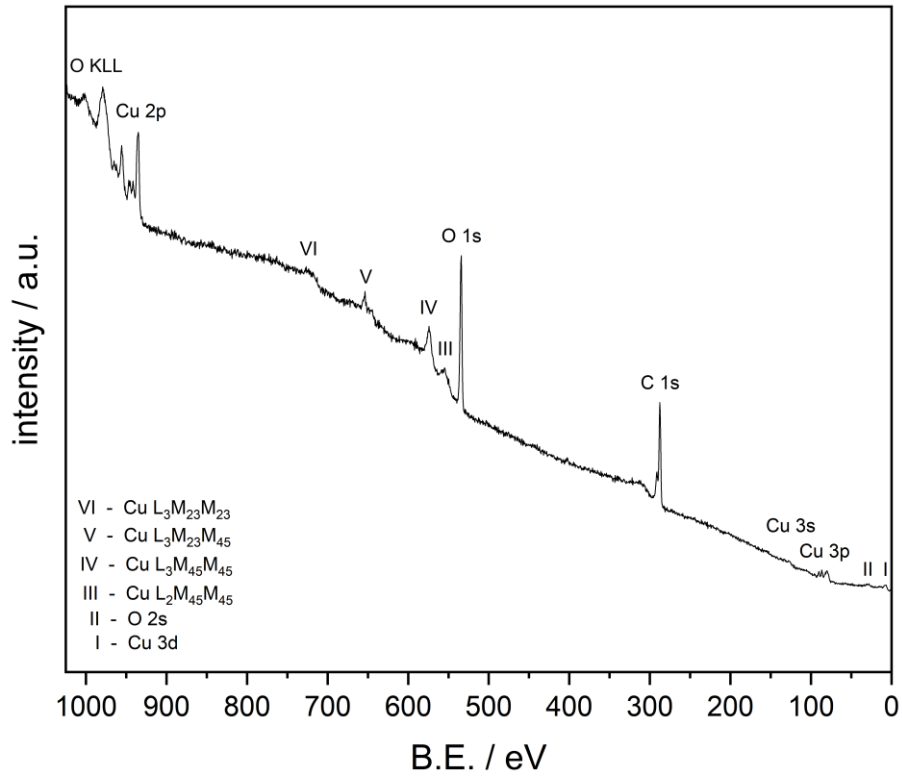

Figure S12. XP survey spectrum of an untreated $Cu_3(btc)_2$ sample with labelled photoelectron and Auger signals.

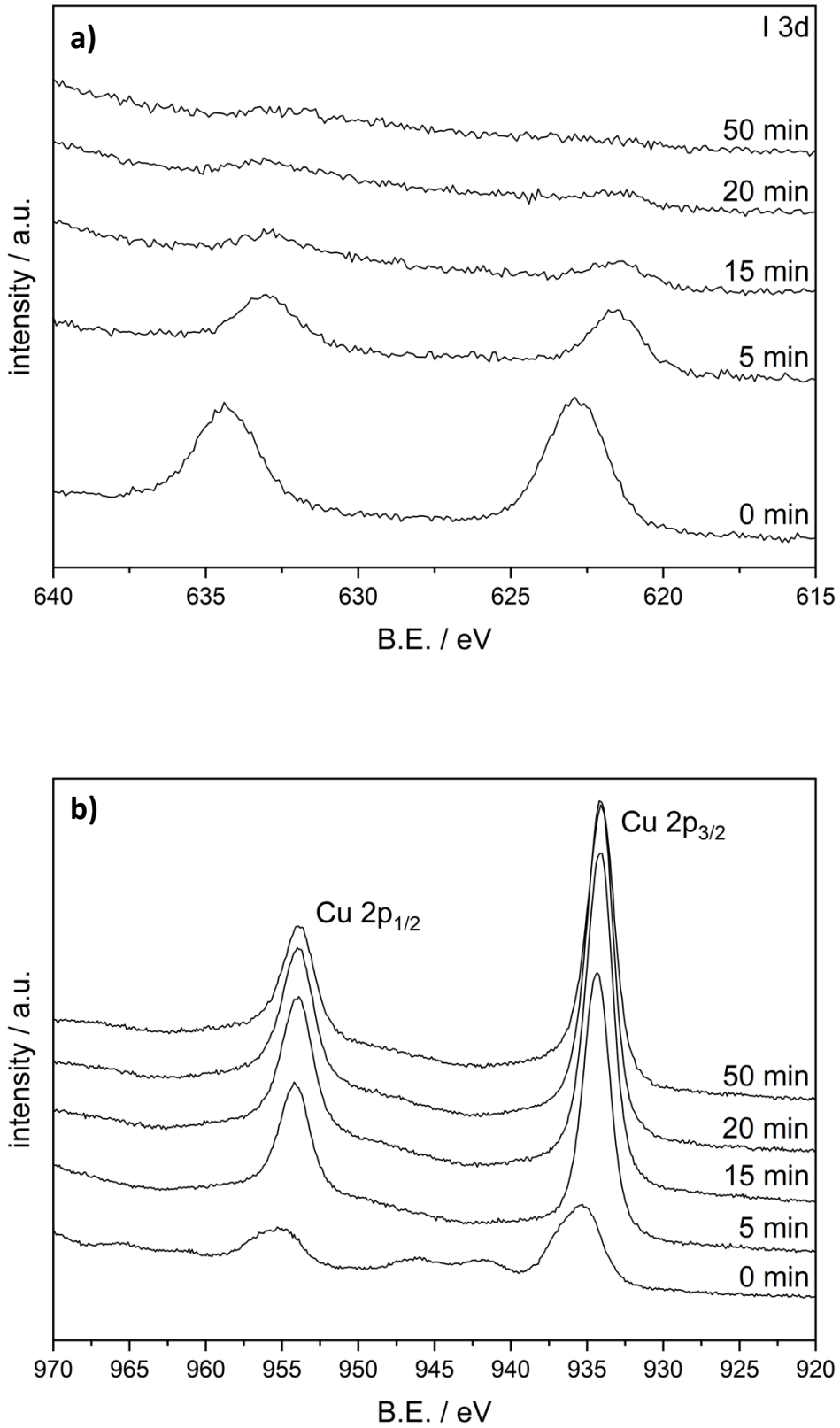

Figure S13. XP core level spectra (vertically offset without background subtraction) of a $[B_{12}I_{11}]^-$ on $Cu_3(btc)_2$ sample acquired after different sputtering processes with Ar^+ ions showing the a) I 3d region and b) Cu 2p region.

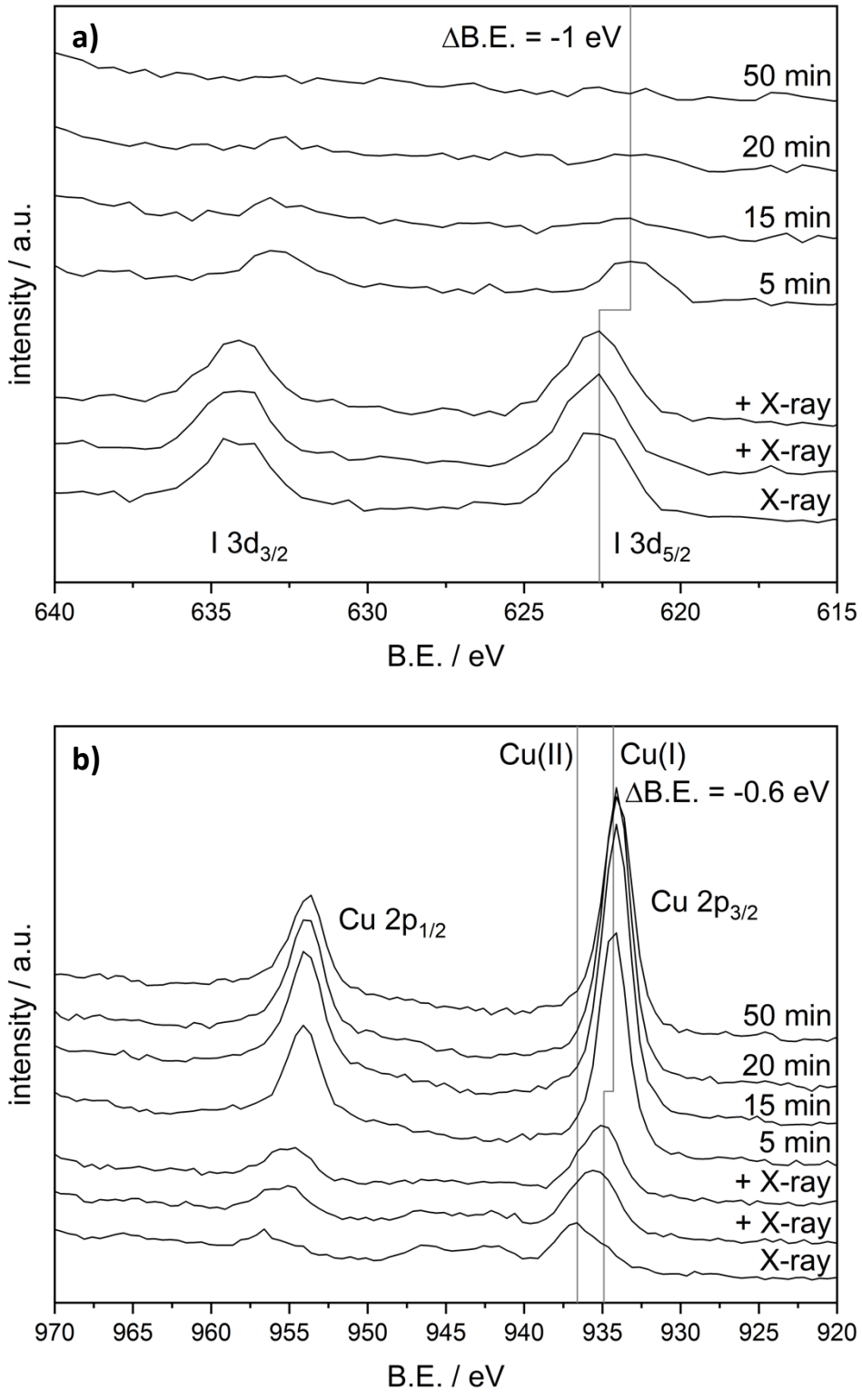

Figure S14. Excerpts of XP survey spectra (vertically offset) of a $[B_{12}I_{11}]^-$ on $Cu_3(btc)_2$ sample acquired after different processes starting with only irradiation with X-rays (increasing irradiation time from bottom to top of the lower three spectra) and afterward sputtering processes with Ar^+ ions based on a) iodine 3d region and b) copper 2p region. The two oxidation states of copper are labelled. The shift in binding energy after the first sputtering process is shown for the a) I $3d_{5/2}$ and b) Cu $2p_{3/2}$ signal.

In order to better understand the changes in binding energies and spectral shapes in Figure S13, additional data are shown in Figure S14. For this figure, excerpts from XP survey spectra with lower resolution are used to also document changes occurring as a result of the irradiation by X-rays. In Figure S14a no changes of the I 3d signal are observed while in Figure S14b the Cu 2p signal shows changes related to the X-ray induced reduction from Cu(II) to Cu(I).[24] The subsequent sputtering causes a binding energy shift for both core levels (and for the C 1s contribution as well). The latter change could be caused by changes in the electrical conductivity of the samples or the charge situation at the surface.

9.1. Estimation of the amount of 1 and 2 on rinsed $Cu_3(btc)_2$ surfaces

We estimated the amount of **1** and **2** on the $Cu_3(btc)_2$ coordination polymer surface after thorough rinsing with EtOH based on the quantification of the I 3d signal (for **1**) and the Ru 3p signal (for **2**) relative to the Cu 2p signal that is assumed to be associated with the substrate. As an important prerequisite, we assume that the whole substrate surface (1x1 cm^2) was initially covered (prior to rinsing) with at least a monolayer of deposited fragment ions after ISL. Furthermore, we assume that the Cu 2p signal intensities are hardly influenced (for $[Ru(bpy)_2]^{2+}$ even less than for $[B_{12}I_{11}]^-$) by the presence of the submonolayer of surface-bound fragment ions after rinsing. We find the following ratios:

For **1**: I 3d/Cu 2p = 0.256 (corresponding to one ion of **1** [with 11 I atoms] per 43 Cu atoms)

For **2**: Ru 3p/Cu 2p = 0.152 (corresponding to one ion of **2** [with 1 Ru atom] per 7 Cu atoms)

From these ratios, we deduce that more **2** than **1** was bound to the $Cu_3(btc)_2$ surface (by factor of 43/7 ≈ 6). This finding is in line with the crater-shaped structure of the electrophilic site of **1** that is sterically more shielded (by large I substituents in its surrounding) compared to the electrophilic site of **2** that is conveniently accessible for bond formation with a carboxylate group of $Cu_3(btc)_2$.

10. LESA mass spectra after ISL of 1 and 2 on $Cu_3(btc)_2$ coordination polymer surfaces

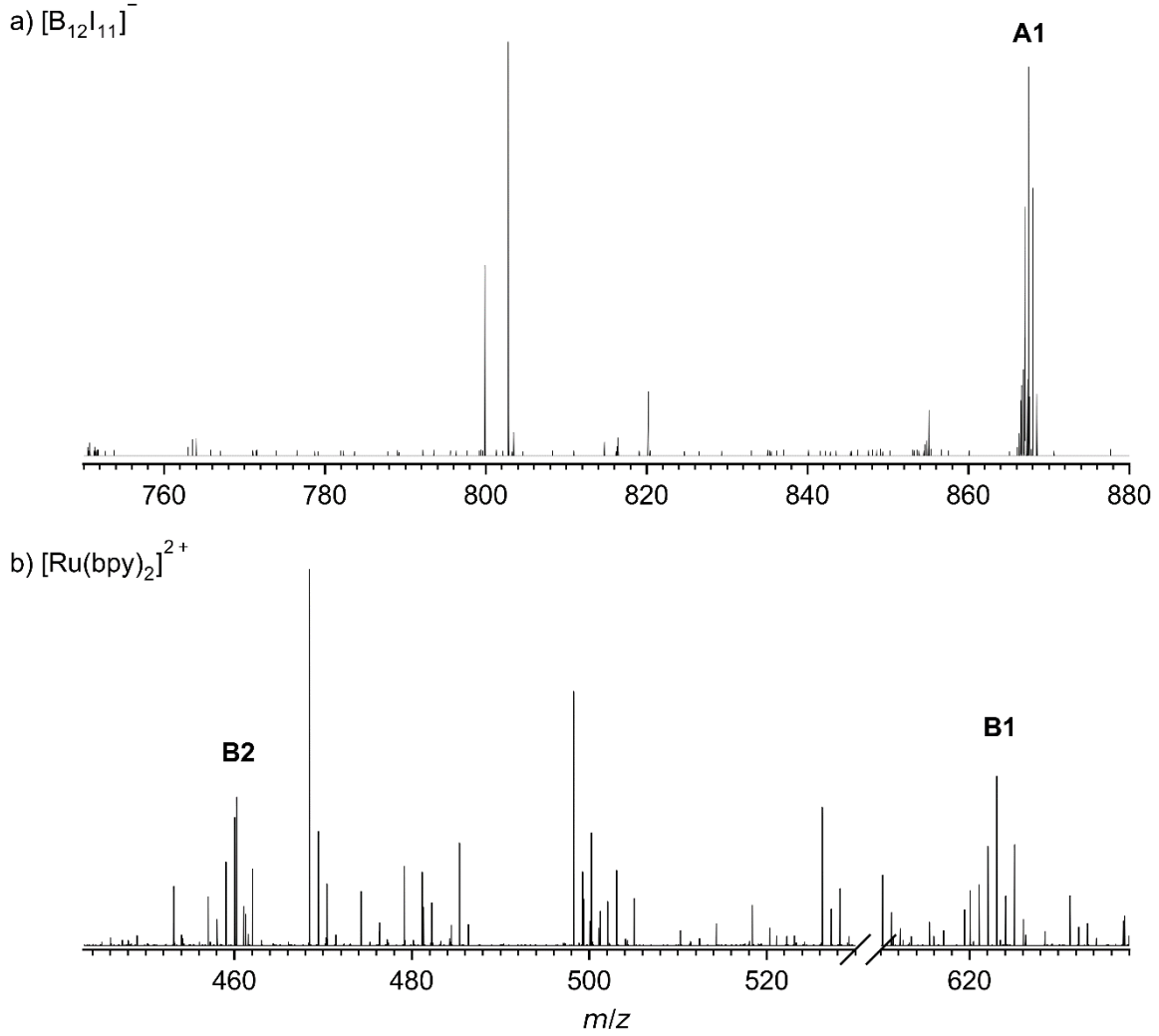

Figure S15. Mass spectrum (MeOH:H_2O 4:1 v/v) acquired with LESA after deposition of a) $[B_{12}I_{11}]^-$ (−ESI) and b) $[Ru(bpy)_2]^{2+}$ (+ESI) on a $Cu_3(btc)_2$ coordination polymer sample (10 layers) that has been rinsed with EtOH after SL.

Table S4. Assignment of LESA-MS signals in Figure S11. m/z *values refer to most abundant signals from the isotopologue distribution.*

Signal	*m/z* (exp.)	*m/z* (sim.) [diff.]	Assignment
$[B_{12}I_{11}]^-$ (**1**)			
A1	867.5146	867.5392 (+0.0246)	$[B_{12}I_{11}(OOCC_6H_3(COOH)_2)]^{2-}$
$[Ru(bpy)_2]^{2+}$ (**2**)			
B1	623.0643	623.0507 (-0.0136)	$[Ru(C_{10}H_8N_2)_2OOCC_6H_3(COOH)_2]^+$
B2	460.0439	460.0348 (-0.0091)	$[Ru(C_{10}H_8N_2)_2NO_2]^+$ (nitrite adduct)

We note that the intensities in the LESA mass spectra acquired from the functionalized $Cu_3(btc)_2$ coordination polymer surfaces were generally low and the abundancies of the trimesate adduct ions **A1** and **B1** were in a range, in which an unambiguous determination of the exact mass is hampered by fluctuations between single mass scans. Also, signals of solvent or surface impurities possess similar intensities and contribute significantly to the obtained spectra. We therefore only perform assignments for signals in Figure S14 that show a characteristic isotopic pattern of either B_{12} (for deposition of **1**) or Ru species (for deposition of **2**) in Table S3. However, Figure S15 shows a *m/z* range in which typical soluble species that form upon ion soft-landing of **1** and **2** would occur (compare Figure S9) in order to rule out that other reaction products of the soft-landed ions and the coordination polymer can be observed. Note that product **B2** (nitrite adduct of **2**) is assumed to be soluble in EtOH since it does not involve a covalent link to the coordination polymer. However, we assume that the porosity of the $Cu_3(btc)_2$ substrate can hinder dissolution of species of suitable size that can be retained in the pores. Product **B2** is consequently also found in the EtOH rinsing solution (see ESI 6).

Figure S16 shows mass spectra of the pure solvent used during LESA-MS (MeOH:H_2O 4:1 *v*/*v*) in order to highlight the contribution of the solvent mixture to the spectra obtained after ISL on $Cu_3(btc)_2$ coordination polymer substrates. Note that the solvent impurities account only partially to the total sum of all impurity signals: Surface impurities must also be considered. For instance, it was shown that common plasticizers (phthalates and adipates) present in the background gas co-accumulate with the deposited ions upon ion soft-landing.[1,8]

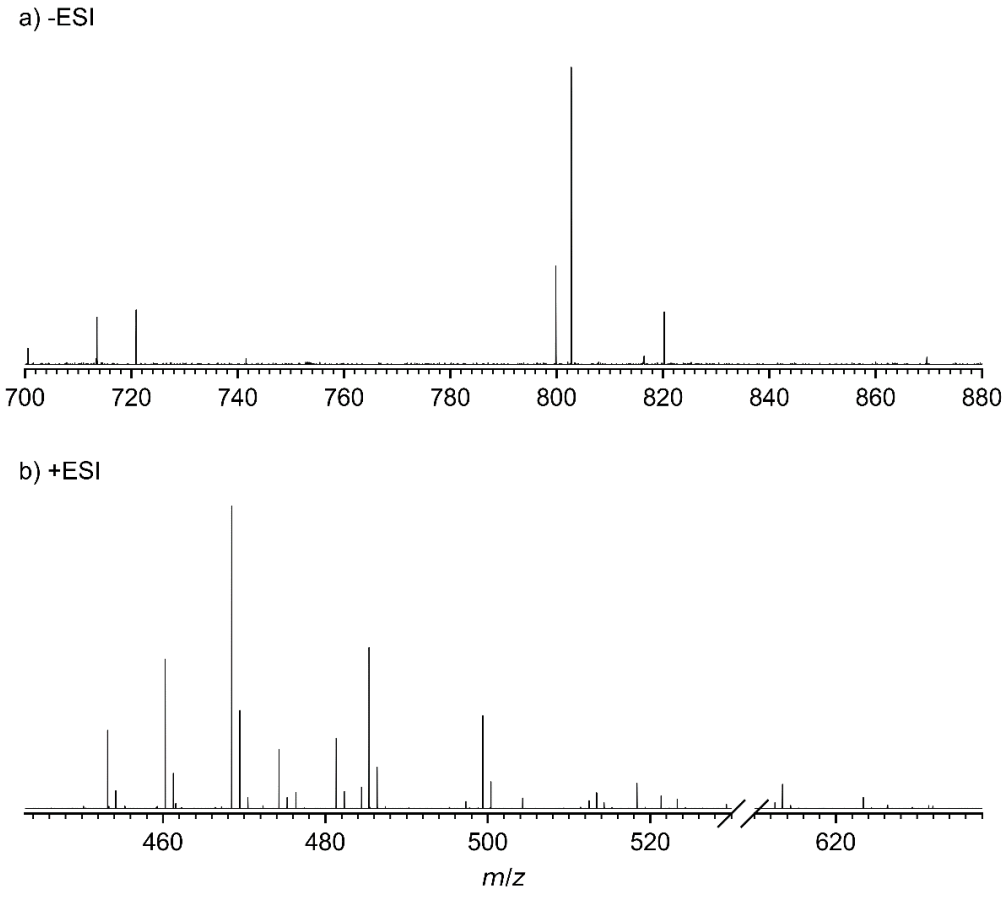

Figure S16. Mass spectra (MeOH:H_2O 4:1 v/v*) acquired with LESA from the pure solvent mixture in a) -ESI and b) +ESI modes in the* m/z *ranges critical for product evaluation (same ranges as in Figure S15).*

11. MS^2 spectrum of B1

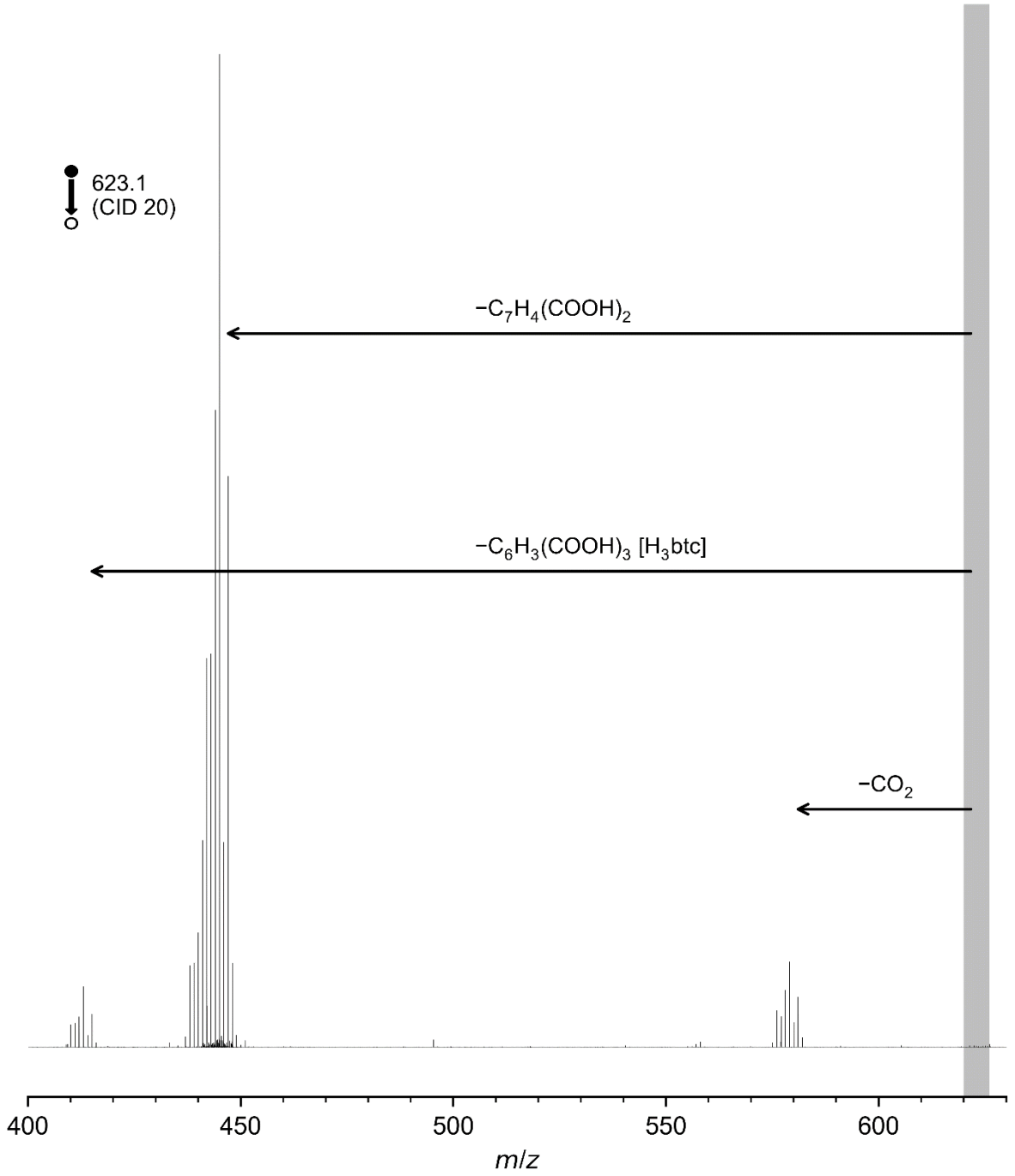

*Figure S17. MS^2 spectrum acquired after isolation and fragmentation of $[Ru(C_{10}H_8N_2)_2OOCC_6H_3(COOH)_2]^+$ ions (Signal **B1**,* m/z 623.1*). Spectral regions of the precursor ions that were isolated and subjected to CID are marked in grey. Eliminations leading to the formation of the major product ions are annotated next to the respective arrows.*

12. LESA mass spectra after ISL of 1 and 2 on deuterated $Cu_3(btc\text{-}d_3)_2$ coordination polymer surfaces

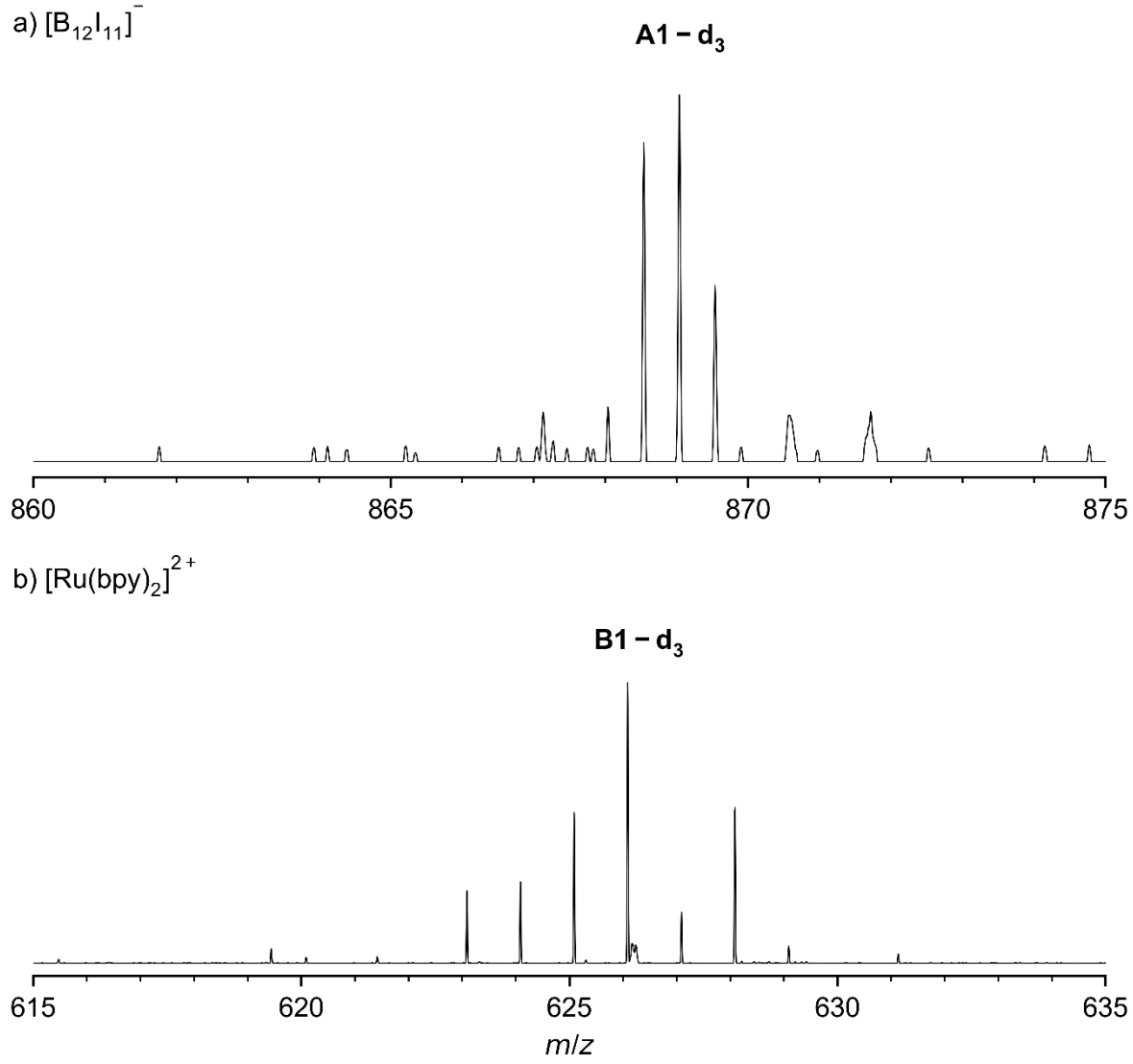

Figure S18. Mass spectrum acquired with LESA (MeOH:H_2O 4:1 v/v) after deposition of a) $[B_{12}I_{11}]^-$ (−ESI) and b) $[Ru(bpy)_2]^{2+}$ (+ESI) on a deuterated $Cu_3(btc\text{-}d_3)_2$ coordination polymer sample (10 layers) that had been rinsed with EtOH after SL. In comparison to Figure S15, all adduct signals are shifted by an amount corresponding to the substitution of 3 H atoms by 3 D atoms towards higher m/z *values, i.e., +* m/z *1.5 in a) and +* m/z *3 in b).*

13. MS^2 spectra of A1-d_3 and B1-d_3

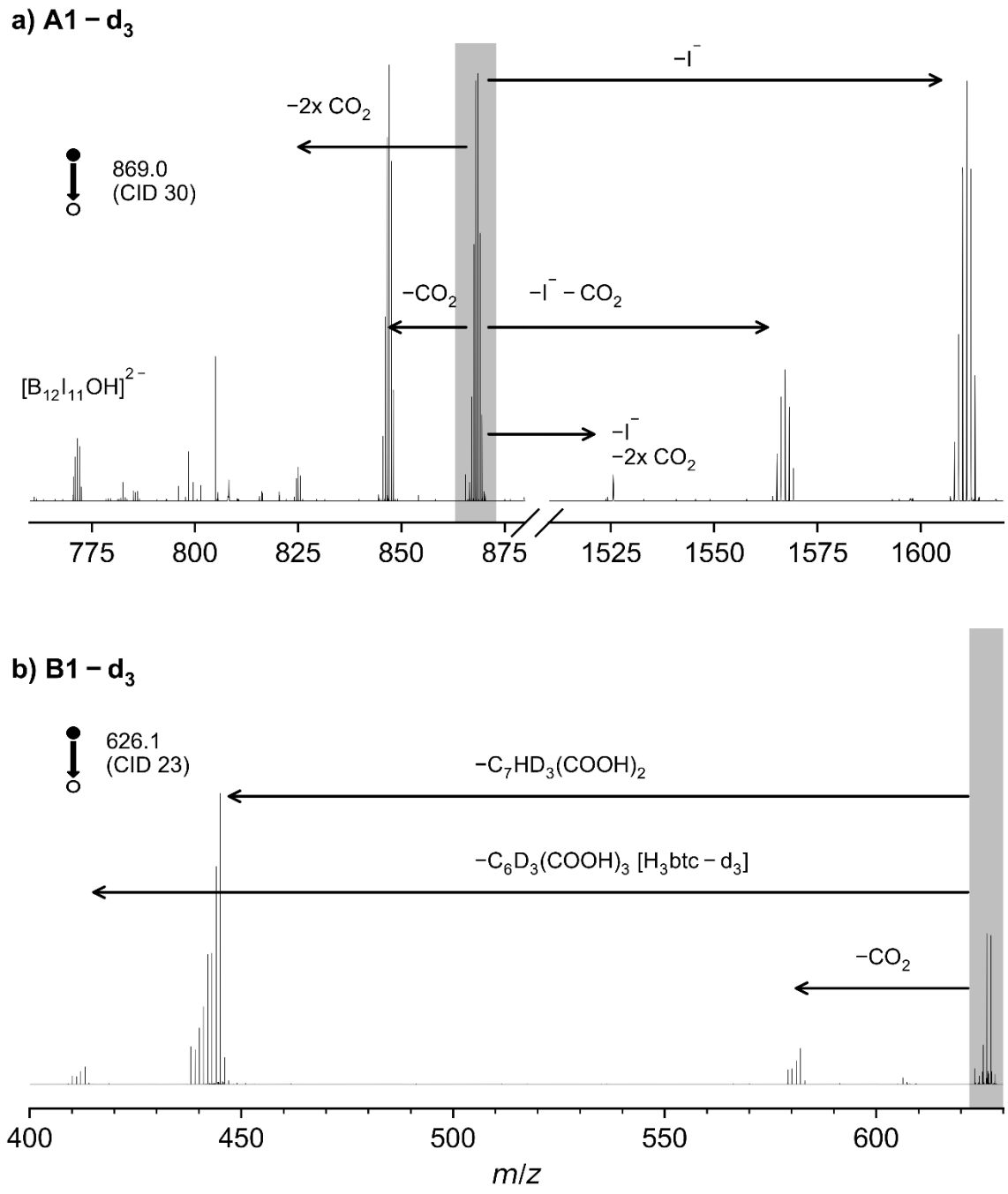

*Figure S19. MS^2 spectra acquired after isolation and fragmentation of a) **A1-d_3** ions and b) **B1-d_3** ions from a $Cu_3(btc)_2$ sample, prepared with btc-d_3 linkers, and on which the **1** and **2** were deposited on, respectively. Spectral regions of the precursor ions that were isolated and subjected to CID are marked in grey. Elimination reactions leading to the formation of the major product ions are annotated next to the respective arrows.*

14. MS^2 spectrum of A2

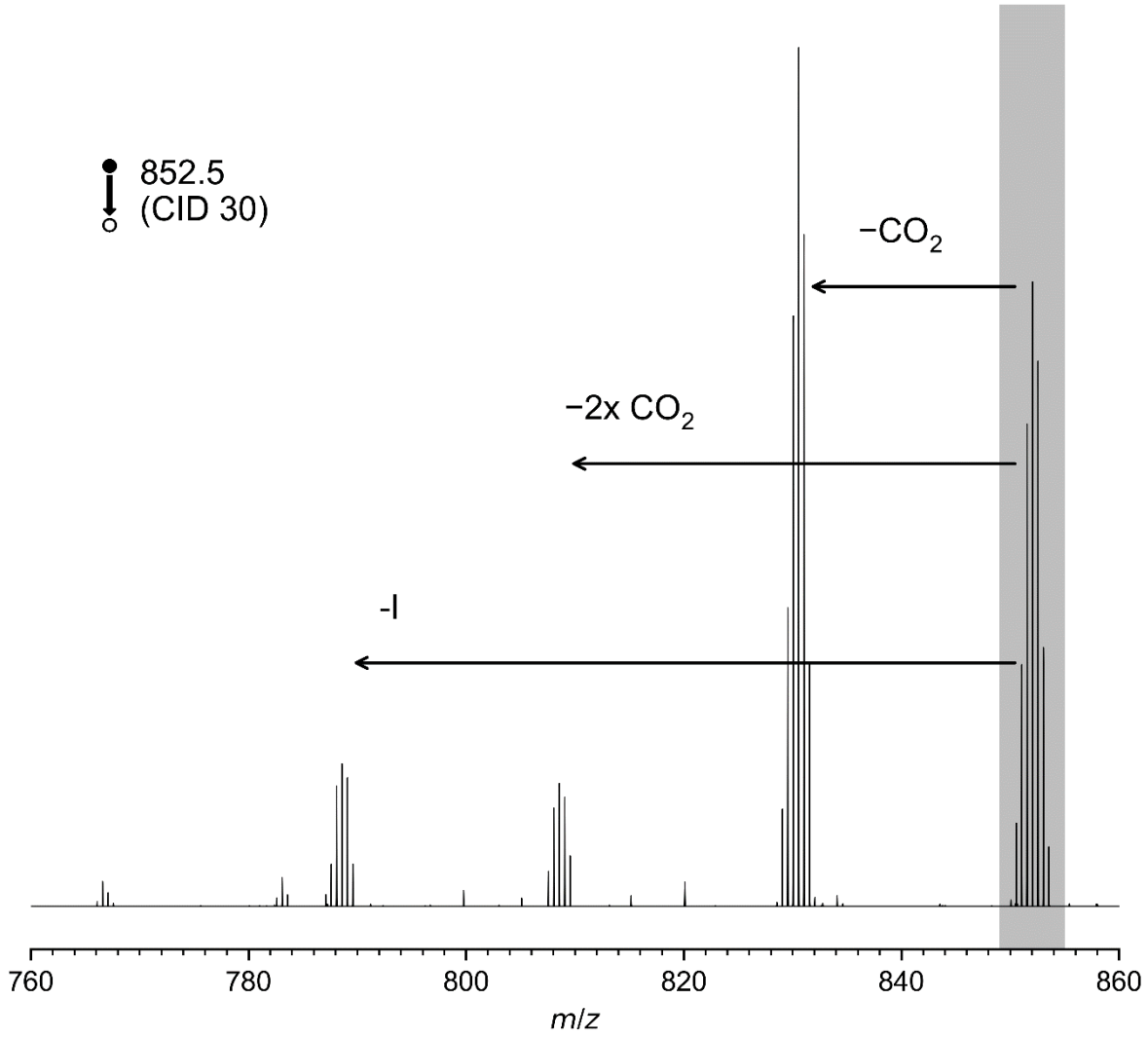

*Figure S20. MS^2 spectrum acquired after isolation and fragmentation of **A2** ions. Spectral regions of the precursor ions that were isolated and subjected to CID are marked in grey. Elimination reactions leading to the formation of the major product ions are annotated next to the respective arrows. Note that the elimination of up to two molecules of CO_2 from **A2** is indicative of bond formation between **1** and the methyl group of MeIp.*

15. ISL of 2 on MeIp-terminated $Cu_3(btc)_2$ samples

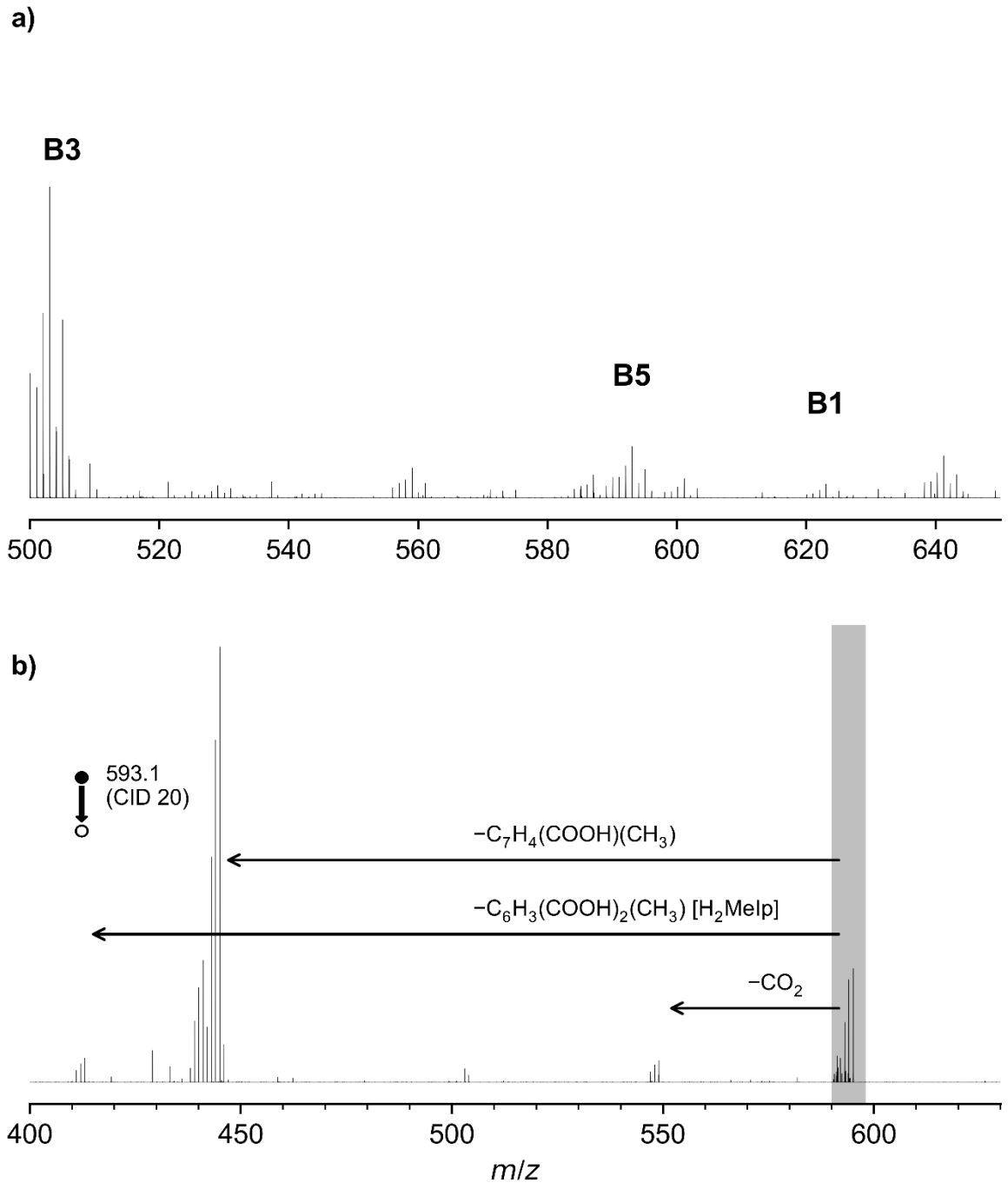

*Figure S21. a) Excerpt of an +ESI mass spectrum of the ethanolic rinsing solution obtained from a 5-MeIp-terminated $Cu_3(btc)_2$ sample onto which **2** was deposited. Aside from negligible amounts of the btc addition product of **2** (**B1**, which can also be found in LESA mass spectra from the rinsed surface) and the lactate adduct of **2** (**B3**), only one additional signal related to MeIp was observed at* m/z *593.1 (**B5**, assigned to $[Ru(C_{10}H_8N_2)_2OOCC_6H_3(COOH)(CH_3)]^+$). Note that the presence of **B5** in the rinsing solution strongly points to the conclusion that during its formation, **2** must have attacked a defectively coordinated MeIp linker. b) MS^2 spectrum obtained after isolation and fragmentation of **B5**, this time obtained during LESA-MS from the rinsed surface. The presence of the very same fragment ion with O_2 bound to the Ru centre as also observed for CID of **B1** (*m/z *445, compare Figure S17) indicates that **2** must have attacked the MeIp linker at an accessible carboxylate group.*

References

1 F. Yang, K. A. Behrend, H. Knorke, M. Rohdenburg, A. Charvat, C. Jenne, B. Abel and J. Warneke, *Angew. Chem. Int. Ed.*, 2021, **60**, 24910–24914.

2 S. Škulj and M. Rožman, *Int. J. Mass Spectrom.*, 2015, **391**, 11–16.

3 E. L. Muetterties, J. H. Balthis, Y. T. Chia, W. H. Knoth and H. C. Miller, *Inorg. Chem.*, 1964, **3**, 444–451.

4 I. Tiritiris and T. Schleid, *Z. Anorg. Allg. Chem.*, 2004, **630**, 1555–1563.

5 K. Ahlenhoff, S. Koch, D. Emmrich, R. Dalpke, A. Gölzhäuser and P. Swiderek, *Phys. Chem. Chem. Phys.*, 2019, **21**, 2351–2364.

6 O. Shekhah, H. Wang, S. Kowarik, F. Schreiber, M. Paulus, M. Tolan, C. Sternemann, F. Evers, D. Zacher, R. A. Fischer and C. Wöll, *J. Am. Chem. Soc.*, 2007, **129**, 15118–15119.

7 H. Y. Samayoa-Oviedo, K.-A. Behrend, S. Kawa, H. Knorke, P. Su, M. E. Belov, G. Anderson, J. Warneke and J. Laskin, *Anal. Chem.*, 2021, **93**, 14489–14496.

8 M. Rohdenburg, Z. Warneke, H. Knorke, M. Icker and J. Warneke, *Angew. Chem. Int. Ed.*, 2023, **62**, e202308600.

9 G. E. Johnson and J. Laskin, *Chem. Eur. J.*, 2010, **16**, 14433–14438.

10 V. Kertesz and G. J. van Berkel, *J. Mass. Spectrom.*, 2010, **45**, 252–260.

11 M. J. Frisch, G. W. Trucks, H. B. Schlegel, G. E. Scuseria, M. A. Robb, J. R. Cheeseman, G. Scalmani, V. Barone, B. Mennucci, G. A. Petersson, H. Nakatsuji, M. Caricato, X. Li, H. P. Hratchian, A. F. Izmaylov, J. Bloino, G. Zheng, J. L. Sonnenberg, M. Hada, M. Ehara, K. Toyota, R. Fukuda, J. Hasegawa, M. Ishida, T. Nakajima, Y. Honda, O. Kitao, H. Nakai, T. Vreven, J. A. Montgomery Jr., J. E. Peralta, F. Ogliaro, M. Bearpark, J. J. Heyd, E. Brothers, K. N. Kudin, V. N. Staroverov, R. Kobayashi, J. Normand, K. Raghavachari, A. Rendell, J. C. Burant, S. S. Iyengar, J. Tomasi, M. Cossi, N. Rega, J. M. Millam, M. Klene, J. E. Knox, J. B. Cross, V. Bakken, C. Adamo, J. Jaramillo, R. Gomperts, R. E. Stratmann, O. Yazyev, A. J. Austin, R. Cammi, C. Pomelli, J. W. Ochterski, R. L. Martin, K. Morokuma, V. G. Zakrzewski, G. A. Voth, P. Salvador, J. J. Dannenberg, S. Dapprich, A. D. Daniels, O. Farkas, J. B. Foresman, J. V. Ortiz, J. Cioslowski and D. J. Fox, *Gaussian16 Revision C.02*, Gaussian, Inc, Wallingford CT, 2019.

12 A. D. Becke, *J. Chem. Phys.*, 1993, **98**, 5648–5652.

13 C. Lee, W. Yang and R. G. Parr, *Phys. Rev. B*, 1988, **37**, 785–789.

14 B. Miehlich, A. Savin, H. Stoll and H. Preuss, *Chem. Phys. Lett.*, 1989, **157**, 200–206.

15 F. Weigend and R. Ahlrichs, *Phys. Chem. Chem. Phys.*, 2005, **7**, 3297.

16 S. Grimme, J. Antony, S. Ehrlich and H. Krieg, *J. Chem. Phys.*, 2010, **132**, 154104.

17 S. Grimme, S. Ehrlich and L. Goerigk, *J. Comput. Chem.*, 2011, **32**, 1456–1465.

18 S. F. Boys and F. Bernardi, *Mol. Phys.*, 1970, **19**, 553–566.

19 S. Simon, M. Duran and J. J. Dannenberg, *J. Chem. Phys.*, 1996, **105**, 11024–11031.

20 F. S. Gentile, M. Pannico, M. Causà, G. Mensitieri, G. Di Palma, G. Scherillo and P. Musto, *J. Mater. Chem. A*, 2020, **8**, 10796–10812.

21 Z. Wang, S. Henke, M. Paulus, A. Welle, Z. Fan, K. Rodewald, B. Rieger and R. A. Fischer, *ACS Appl. Mater. Inter.*, 2020, **12**, 2655–2661.

22 G. Delen, Z. Ristanović, L. D. B. Mandemaker and B. M. Weckhuysen, *Chem. Eur. J.*, 2018, **24**, 187–195.

23 N. R. Dhumal, M. P. Singh, J. A. Anderson, J. Kiefer and H. J. Kim, *J. Phys. Chem. C*, 2016, **120**, 3295–3304.

24 M. A. Newton, A. J. Knorpp, J. Meyet, D. Stoian, M. Nachtegaal, A. H. Clark, O. V. Safonova, H. Emerich, W. van Beek, V. L. Sushkevich and J. A. van Bokhoven, *Phys. Chem. Chem. Phys.*, 2020, **22**, 6826–6837.